RSC Advances

PAPER

View Article Online
View Journal | View Issue

Cite this: *RSC Adv.*, 2023, **13**, 27512

Engineered rare-earth nanomaterials for fluorescence imaging and therapy†

Hongru Wang,[ab] Zheng Wei,[c] Yangyang Zhao,[e] Shidong Wang,[*d] Lili Cao,[*b] Fan Wang,[c] Kai Liu[ce] and Yanfei Sun[*c]

Received 15th April 2023
Accepted 26th August 2023

DOI: 10.1039/d3ra02503a

rsc.li/rsc-advances

Early diagnosis and treatment are of great significance for hindering the progression of brain disease. The limited effects of available treatments and poor prognosis are currently the most pressing problems faced by clinicians and their patients. Therefore, developing new diagnosis and treatment programs for brain diseases is urgently needed. Near-infrared (NIR)-light-responsive, lanthanide-doped upconversion nanoparticles (UCNPs) provide great advantages both in diagnosis and therapy. Hence, we synthesised nanoparticles comprised of a UCNPs core with surface functionalization. UCNPs@Au was used for NIR fluorescence imaging in the brain and inhibiting the growth of mouse glioma 261 (GL261) cells depending on photothermal properties. In addition, a UCNPs core and a mesoporous silica layer as the outer shell with a tannic acid–Al^{3+} ions (TA–Al) complex as a "gatekeeper" were used for pH-triggered doxorubicin/small interfering ribonucleic acid delivery *in vitro*. Based on our preliminary results, we expect to develop more multifunctional nanoscale diagnostic and therapeutic agents based on UCNPs for the diagnosis and treatment of brain diseases, including Alzheimer's disease, Parkinson's disease, and brain tumours.

Introduction

The brain is the most structurally complex organ in the body for controlling the entire functioning of an organism. Due to the technological limitations of currently available imaging tools, our understanding of the brain is still incomplete, and brain disease has always been and continues to be a huge problem threatening human health.[1,2] For example, the specific pathogenesis of common brain diseases, such as Alzheimer's disease[3] and brain tumours,[4] is still unclear. Early diagnosis and therapy remarkably improve the quality of life of patients with brain diseases. However, the limited efficacy and poor prognosis of traditional drugs pose major challenges to clinicians in diagnosing and prescribing appropriate therapeutic measures for these brain diseases[5–7]. Therefore, developing new strategies for the treatment of brain diseases is urgently needed.

Nanomaterials have attracted increasing amounts of attention in the field of precision medicine and clinical transformation of brain diseases.[8–11] The selective functionalisation of nanocarriers bearing fluorescent molecules and drugs to build a multifunctional nano platform has ushered in a new dawn for brain diseases in the diagnosis and therapy. As one of the important components of the nano diagnosis and treatment platform, fluorescence molecular imaging technology can realise multi-level imaging from cell to body and provide more disease information for early clinical diagnosis. In the past, single-mode imaging based on a single imaging probe could only provide low resolution and weak tissue penetration, negatively affecting the detection rate of disease and formal diagnosis. However, in order to break through the limit of single-mode imaging, multiple imaging probes are required to achieve multimodal imaging for brain diseases. To that end, lanthanide-doped upconversion nanoparticles (UCNPs) are one potential solution for their excellent optical properties, strong X-ray attenuation and special magnetic properties.[12] For this, they have already been widely used in the biomedical imaging field.[13] In particular, upconversion luminescence (UCL) imaging shows great advantages with little autofluorescence signal and high signal-to-noise ratio at high depth of penetration.[14] These properties indicate that the UCL imaging approach is especially suitable for tracking and labelling biomolecule of the brain. Furthermore, it also has been combined with photothermal therapy (PTT).[15] For this, it should be noted that Au nanoparticles have emerged as the

[a]*Department of Neurology, Liaocheng People's Hospital, Liaocheng, Shandong, 252000, China*

[b]*Department of Neurology, Qilu Hospital of Shandong University, Jinan, Shandong, 250012, China. E-mail: qilucll@163.com*

[c]*State Key Laboratory of Rare Earth Resource Utilization, Changchun Institute of Applied Chemistry, Chinese Academy of Sciences, Changchun 130022, China. E-mail: Sunyf90@163.com*

[d]*Musculoskeletal Tumor Center, Peking University People's Hospital, Beijing, 100044, China. E-mail: stonewang@bjmu.edu.cn*

[e]*Department of Chemistry, Tsinghua University, Beijing 100084, China*

† Electronic supplementary information (ESI) available. See DOI: https://doi.org/10.1039/d3ra02503a

potential agents of PTT due to their outstanding light-to-heat conversion[16] and chemical stability. UCNPs@Au nanoparticles specifically have been used to treat skin cancer because of the aforementioned excellent light-to-heat conversion property.[15] Therefore, it is worth exploring further the application of nanoprobes based on the preparation of UCNPs and Au nanoparticles in the diagnosis and treatment of brain diseases.

Current therapies for brain disease, including surgical resection, small molecular drugs, and gene therapy, have substantial limitations, such as poor drug delivery effect, rapid degradation, and serious damage.[17,18] Rare earth luminescent materials can also be used as drug carriers to deliver drugs to diseased tissues for the treatment of diseases. For example, UCNPs have been employed as anti-cancer drugs or small interfering ribonucleic acid (siRNA) nanocarriers in disease treatment.[19,20] However, it is necessary to avoid the early release of anti-cancer drugs to diseased tissues to increase the efficacy of the treatment. A large number of studies have demonstrated that a stimuli-responsive strategy, such as pH, light, and temperature, can realise on-demand drug release.[21–23] Notably, metal–phenolic networks (MPNs) composed of natural polyphenols (*e.g.*, tannic acid) and metal ions were shown to be degraded in acidic environments.[24–26] Significantly, the degrading mechanism for the MPNs networks are relatively stable at the pH of the bloodstream (7.4), and progressively degrade at lower pH environments values.[26] Moreover, the MPNs networks have high mechanical stability and good biocompatibility, which make them the perfect "gatekeepers" for pH-triggered drug delivery. Herein, it is worth further exploring this application by combining a mesoporous silica shell and MPNs networks with UCNPs for the therapy in brain diseases. To this end, we have reasonably designed and assembled a new rare earth nanoparticle system with both diagnostic and treatment functions.

Experimental section

Chemicals

We purchased $ReCl_3$, oleic acid (OA), 1-octadecene (ODE), NaOH, NH_4F, polyethyleneimine (PEI) (M_w = 1800), $HAuCl_4 \cdot 4H_2O$, tetraethyl orthosilicate (TEOS), *N*-2-hydroxyethylpiperazine-*N*-2-ethane sulfonic acid (HEPES), tannic acid (TA), and the 3-aminopropyltriethoxysilane (APTES) from Aladdin (Shanghai, China). Hexadecyl trimethyl ammonium bromide (CTAB), ethanol, and aluminium trichloride were purchased from Sinopharm Chemical Reagent. Doxorubicin (Dox) was purchased from Sigma–Aldrich. Diethypyrocarbonate water (DEPC) and siRNA were procured from Sangon Biotech. Mouse embryonic fibroblast cell lines (NIH-3T3), mouse glioma 261 (GL261), Dulbecco's modified eagle medium (DMEM), phosphate buffered saline (PBS), penicillin, streptomycin, and foetal bovine serum (FBS) were purchased from Keygen Biotechnology (Nanjing, China). Cell counting kit-8 (CCK8) and calcein-acetoxymethyl (AM)/propidium iodide (PI) co-stain were bought from Solarbio.

Animals

Male BALB/c57 mice (5–6 weeks) were bought from the Changchun Institute of Applied Chemistry, Chinese Academy of Sciences (Changchun, China). All animal experiments were conducted in compliance with the Animal Management Rules of the Ministry of Health of the People's Republic of China and with the approval of the Institutional Animal Care and Use Committee of the Animal Experiment Center of Peking University People's Hospital.

Preparation of UCNPs

The UCNPs ($NaYF_4$: Yb, Er) cores were synthesized as follows. 1×10^{-3} mol $RECl_3$ (RE = Y, Yb and Er, Y : Yb : Er = 78 : 20 : 2), 6 mL OA, and 18 mL ODE were mixed, and the system was heated to 160 °C under inert gas. This temperature was maintained for 40 min and then dropped to 50 °C. 0.1 g NaOH and 0.148 g NH_4F dissolved in 12 mL methanol solution was added into the system with stirring for 2 h. Next, the system was heated to 100 °C until the methanol was evaporated, and the temperature was raised to 300 °C for 1 h. Finally, the products were purified with anhydrous ethanol and cyclohexane three times. Similarly, the core–shell ($NaYF_4$:Yb, Er@$NaYF_4$) was also synthesised using the same method and the products were re-dispersed in 10 mL cyclohexane for later use.

Preparation of UCNPs@Au

UCNPs@PEI was first prepared. Ligand-free UCNPs was acquired by removing the oleate ligands with hydrochloric acid. Then, ligand-free UCNP was mixed with 100 mg PEI added into 10 mL deionized water for 12 h under stirring. Afterwards, we used ethanol and deionized water to elute the obtained mixture. Finally, 130 mg $HAuCl_4 \cdot 4H_2O$ added into 10 mL deionized water was mixed with UCNPs@PEI and heated to 70 °C for 5 min. These obtained products were centrifuged and dried for later use.

Preparation of UCNPs@mSiO$_2$

Hydrochloric acid was used to remove the oleate ligands of the UCNP and then stirred with 0.1 g CTAB solution overnight. Followed by the addition of 6 mL ethanol, 100 μL NaOH solution (2 M) and 80 μL TEOS dissolved in 1 mL ethanol, the mixture was stirred for 1 h at 60 °C. Next, 20 μL of APTES dissolved in 1 mL ethanol was added into the mixture under stirring for another 30 min. In order to reduce the cytotoxicity, we remove the extra CTAB in ammonium chloride alcohol solution. The resultant UCNPs@mSiO$_2$–NH$_2$ compound was purified with ethanol three times and dried for later use.

Preparation of UCNPs@mSiO$_2$–Dox/siRNA@TA–Al

UCNPs@mSiO$_2$ solution was mixed with TA (10 μL, 24 mM) and $AlCl_3$ (10 μL, 24 mM), followed by a quick vortex for 20 s, respectively. 0.1 M HEPES was used to adjust the pH to 7.0. For Dox loading, UCNPs@mSiO$_2$ solution (10 mg mL^{-1}) was mixed with Dox solution (1 mg mL^{-1}) and stirred for 24 h. For siRNA loading, 10 mg of UCNPs@mSiO$_2$ dispersed in 1 mL DEPC water was mixed with siRNA aqueous solution (20 pmol μL^{-1})

and stirred for 4 h. Finally, UCNPs@mSiO$_2$–Dox@TA–Al and UCNPs@mSiO$_2$–siRNA@TA–Al nanoparticles were purified with deionized water for later use.

Materials characterization

Transmission Electron Microscopy (TEM) was performed with a JEOL-2010 transmission electron microscope (JEOL Co., Japan). Fourier Transform Infrared (FTIR) spectroscopy was performed with a PerkinElmer 580B IR spectrophotometer (PerkinElmer, USA). Powder X-ray Diffraction (XRD) was performed with a D8 Focus diffractometer (Bruker Co., Germany). Zeta-potential was measured by a Zetasizer Nano ZS (Malvern Instruments Ltd., UK). Ultraviolet-Visible (UV-Vis) absorption spectra was recorded using a Shimadzu UV-3600 spectrophotometer (Shimadzu Co., Japan). Inductively coupled plasma mass spectrometry (ICP-MS) analysis was performed with an ELAN 9000/DRC ICP-MS system (PerkinElmer, USA). Fluorescence spectra was acquired with a modular spectrofluorometer using Fluorolog-3 (Horiba Jobin Yvon, France). Nitrogen adsorption–desorption isotherms were determined using an Accelerated Surface Area and Porosimetry System (ASAP2020M).

Photothermal effects

Aqueous suspension of UCNPs@Au (2 mg mL^{-1}) in the cuvette was analysed with an incident 980 nm laser to evaluate its *in vitro* photothermal performance. A 980 nm laser (4.458 W cm^{-2}) was applied for 15 min, and another test of 6 min was performed for cooling without the laser. The test of water was conducted for 12 min with a 980 nm laser as a control. UCNPs@Au (2 mg mL^{-1}) was microinjected into the striatum of the mice brains (anteroposterior, 0 mm; mediolateral, −2 mm; dorsoventral, −3.75 mm relative to bregma) to evaluate its *in vivo* photothermal performance. The temperature was monitored by an FLIR A × 5 camera with a 980 nm laser 5 min later.

Cell culture

The NIH-3T3 and GL261 cells were cultured in a DMEM medium containing 10% FBS and 1% antibiotics (penicillin–streptomycin, 10 000 U mL^{-1}) at 37 °C and 5% CO_2.

Cytotoxicity measurement

The NIH-3T3 cells were cultured in 96-well plates. After cultured for 12 h, different concentrations of UCNPs@Au and UCNPs@mSiO$_2$@TA–Al (dosages: 0, 12.5, 25, 50, 100, 200, and 400 μg mL^{-1}) were added in glucose-free DMEM cultured for 24 h. Finally, we evaluated the cytotoxicity by CCK-8 assay. Then the data were measured at 450 nm absorbance.

Anti-tumour efficacy *in vitro*

The GL261 cells were inoculated in 96-well plates. After cultured for 12 h, different concentrations of UCNPs@Au (dosages: 3.125, 6.25, 12.5, 25, 50, 100 μg mL^{-1}) were added in glucose-free DMEM cultured for 24 h. A 980 nm laser was applied for 5 min. Afterwards, the anti-tumour efficacy was tested by CCK-8 assay.

Calcein-AM/PI co-staining

GL261 cells were cultured in 24-well plates for 12 h. Then, UCNPs@mSiO$_2$–Dox@TA–Al (100 μg mL^{-1}) were added to further incubate the cells for 48 and 72 h. Cells were stained with calcein AM for 1 h and PI for 1 min, followed by washing with PBS. Finally, the cellular modality of these cells was monitored using fluorescence microscopy.

Imaging of UCNPs@Au in the brain

UCNPs@Au (2 mg mL^{-1}) and PBS (as a control) solutions were microinjected into the striatum of the mice's brains. The mice were imaged using a Maestro (CRi) imaging system 5 min later. The settings of excitation were at 980 nm and emission were at 540 nm for fluorescence measurements.

pH-responsive drug release

UCNPs@mSiO$_2$–Dox@TA–Al dispersed in PBS (10 mM, pH 5.0, 6.0) solutions were performed with gentle shaking at 37 °C to detect the pH-responsive Dox release. The nanoparticles were centrifuged, the supernatant was collected at selected time intervals (0, 6, 24, 48, and 72 h), and the precipitate was redispersed in accordance with the method above. The cumulative amount of Dox released in the PBS at each predetermined time interval was analysed by UV-vis spectroscopy. As for pH-responsive siRNA release, the same method was used to analyse the siRNA release at selected time intervals (4, 8, and 12 h) using gel electrophoresis.

Statistical analysis

All data were analyzed using GraphPad Prism Software Version 7 and Origin 2018.

Results

Schematic for the article

Therefore, based on the multifunctional nano-enabled theranostic agent UCNPs, combined with near-infrared (NIR) fluorescence imaging and drug loading, we synthesized UCNPs@Au nanomaterials to realise brain imaging by UCL. In addition, we developed the UCNPs@mSiO$_2$@TA–Al nanomaterials, consisting of UCNPs core, the mesoporous silica layer and TA–Al as a "gatekeeper" for pH-triggered Dox/siRNA delivery (Fig. 1).

Preparation and characterization of the UCNPs@Au nanoparticles

The NaYF$_4$:Yb,Er@NaYF$_4$ (UCNPs) were synthesized by a solvent thermal method.[27] The core was prepared with NaYF$_4$ nanoparticles co-doped with Yb^{3+} and Er^{3+}, and monodispersed NaYF$_4$ coated the shell. UCNPs@Au nanoparticles were formed by a ligand exchange process using PEI, which occurred as a redox reaction with HAuCl$_4$ (Fig. S1†). The size and appearance of the UCNPs and UCNPs@Au were determined through TEM (Fig. 2a), and a mean diameter of 30.71 nm was calculated of UCNPs@Au. The zeta potential of ligand-free UCNPs was 12.8 mV. Au attachment to nanoparticles induced a decline in

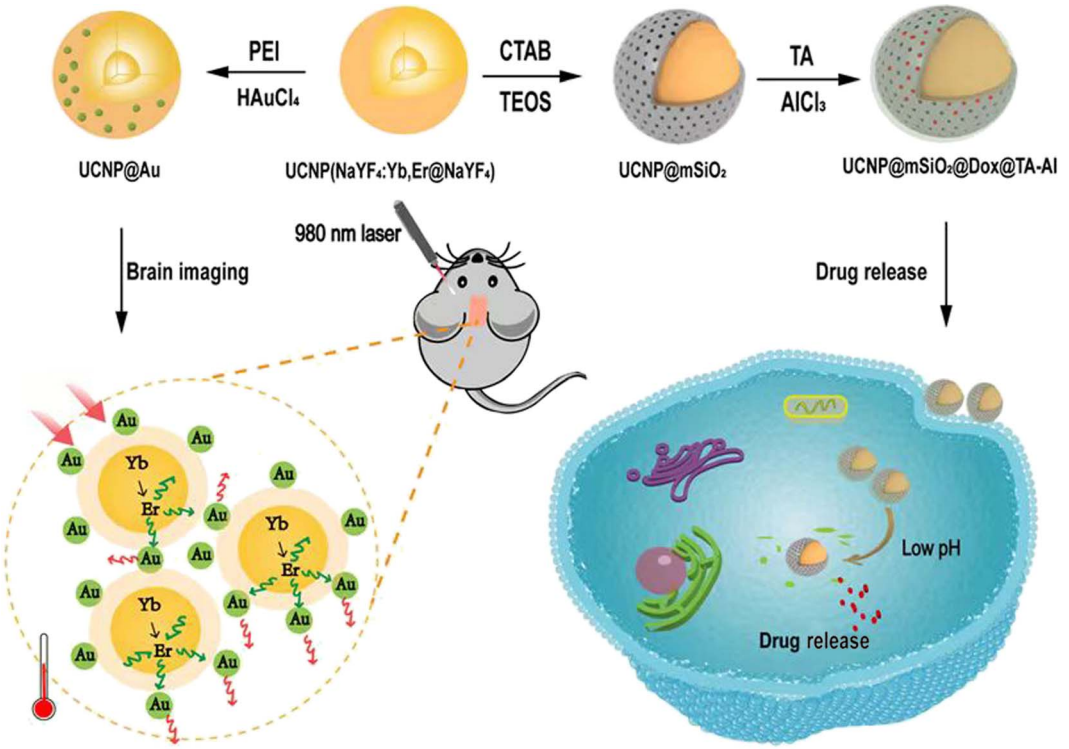

Fig. 1 Schematic showing the synthesis of the UCNPs@Au and UCNPs@mSiO$_2$–Dox@TA–Al. The multifunctional nano agents were used for UCL imaging and the monitoring of pH-responsive drug release.

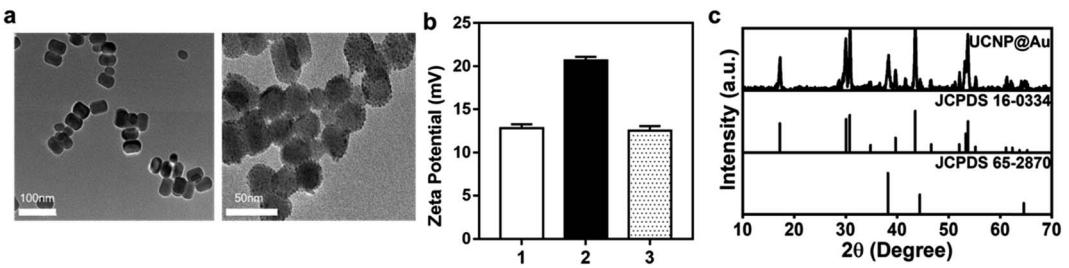

Fig. 2 Preparation and characterization of the UCNPs@Au. (a) TEM analysis of the core–shell UCNPs (NaYF$_4$:Yb, Er@NaYF$_4$) and UCNPs@Au. Scale bar: 100 nm, 50 nm. (b) Zeta potentials of different samples (1: ligand free UCNP; 2: UCNPs@PEI; 3: UCNPs@Au). (c) XRD spectra of UCNPs@Au, standard card of β-NaYF$_4$ (JCPDS no. 16-0334), and Au (JCPDS no. 65-2870).

the zeta potential, as understood by comparing the values for UCNPs@PEI (20.67 mV) and UCNPs@Au (12.5 mV), confirming the successful synthesis of the latter (Fig. 2b). Also, through ICP-MS analysis, it was determined that 1.0 mg UCNPs@Au contains 19.1 μg Au, which further confirmed the attachment of the Au nanoparticles onto the UCNPs (Table 1). The XRD spectrum of the UCNPs@Au are consistent with the standard cards of both β-NaYF$_4$ (JCPDS no. 16-0334) and Au (JCPDS 65-2870), which verified the co-existence of β-NaYF$_4$ and Au (Fig. 2c).

Photothermal effect and UCL imaging of the UCNPs@Au

Subsequently, fluorescence imaging of the UCNPs@Au was investigated. Upconversion fluorescence emission spectra were collected for UCNPs and UCNPs@Au excited with a NIR illumination at 980 nm. Upon excitation at 980 nm, the spectra show output signals for characteristic UCL emissions from Er^{3+} at 525, 540, and 650 nm, which can confirm UCL imaging optically (Fig. 3a). The UV-vis-NIR spectra of UCNP@Au showed a strong absorption at 540 nm, resulting from the plasma resonance absorption peak of isotropous Au NPs (Fig. S2†). As Au nanoparticles had a strong absorption at 540 nm and short distance from the UCNPs, fluorescence measurements might indicate that a certain proportion of fluorescence resonance energy transfer emerged with the illumination of 980 nm laser.[28] In order to further study this phenomenon, the photothermal effect of UCNPs@Au (2 mg mL^{-1}) increased to ≈49.4 °C in 15 min with 980 nm laser (Fig. 3b) and the photothermal conversion efficiency (η) was calculated to be 23.3% (Fig. S3†). As NIR irradiation offers a higher depth of tissue penetration,

Table 1 ICP-MS analysis of UCNPs@Au

ICP-MS	Yb	Er	Au
Atomic weight (g mol^{-1})	173	167.3	197
Mass (ppm)	55.34	3.924	133.5
Molar (mM)	0.3199	0.0235	0.6777

we further investigated the photothermal effect in the brains of mice. The temperature of captured thermal images in UCNPs@Au-injected mice was significantly increased to 63.4 °C under 980 nm laser illumination compared with the controls (Fig. 3c). The upconverted emission signals were monitored through *in vivo* fluorescence imaging of the mice brains, as shown in Fig. 3d. The UCNPs@Au (2 mg mL^{-1}) fluoresced strongly in comparison to the controls. In addition, the biosafety of UCNPs@Au was assessed in a NIH-3T3 cell line using the CCK-8 assay; 73% of cells remained alive after exposure to the UCNPs@Au (50 μg mL^{-1}) (Fig. S4†). In the end, UCNPs@Au has certain advantages in the treatment of brain gliomas. GL261 cells were incubated with UCNPs@Au and inhibited the growth of glioma cells under the 980 nm laser under different concentrations (Fig. S5†).

Characterization of the UCNPs@mSiO$_2$@TA–Al and the sustained-release properties of the anti-cancer drug

Next, we further examined the characteristics of the UCNP core for drug loading. First, we developed UCNPs described above, followed with the mesoporous silica as a shell for drug loading. Surface functional modification with biodegradable complex of TA–Al was performed to achieve a pH-responsive drug delivery (Fig. 1). The detailed procedure of the UCNPs@mSiO$_2$–Dox@TA–Al is shown schematically in Fig. 1. First, the NaYF$_4$:Yb, Er@NaYF$_4$ (UCNPs) was synthesized as described. Then, the mesoporous silica shell was coated onto the surface of UCNPs followed by the APTES-modified UCNPs@SiO$_2$. The formation of the amino group and Si–O–Si frameworks were evidenced by FTIR spectroscopy (Fig. S6†). The Brunauer–Emmett–Teller surface area (577.4696 m^2 g^{-1}), pore volume (0.389011 cm^3 g^{-1}), and pore size (2.5 nm) of UCNPs@mSiO$_2$ were evidenced by nitrogen adsorption–desorption testing (Fig. S7 and S8†). Through TEM analysis, it was determined that the mean size of the prepared UCNPs@mSiO$_2$ grown to 66.4 nm (Fig. 4a). Next, Dox/siRNA was loaded into the nanoparticles adopting a method of plain physisorption, followed by functionalization of the TA–Al complex to hold the drug in the mesopores. Through ICP-MS analysis, it was determined that 1.0 mg UCNPs@mSiO$_2$@TA–Al contained 82.18 μg Si and 1.95

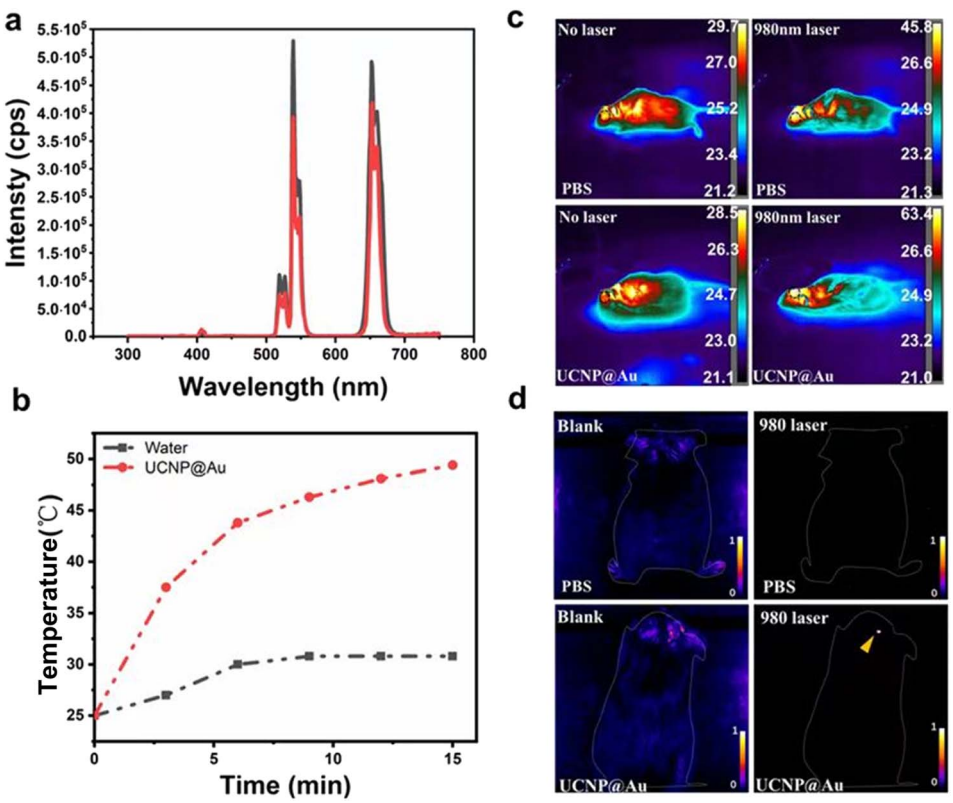

Fig. 3 Photothermal effect and UCL imaging of the UCNPs@Au. (a) Upconversion fluorescence emission spectra of UCNPs (black) and UCNPs@Au (red) excited with NIR illumination at 980 nm. (b) Photothermal testing *in vitro* of the UCNPs@Au and water as the control with 980 nm NIR laser. (c) Thermal images of different groups *in vivo*: PBS injection with no laser, PBS injection with 980 nm laser; UCNPs@Au nanoparticle injection with no laser; UCNPs@Au nanoparticle injection with 980 nm laser. (d) The upconverted emission signals were checked for fluorescence imaging of the mice brains with different groups (PBS injection with no laser; PBS injection with 980 nm laser; UCNPs@Au injection with no laser; UCNPs@Au injection with 980 nm laser).

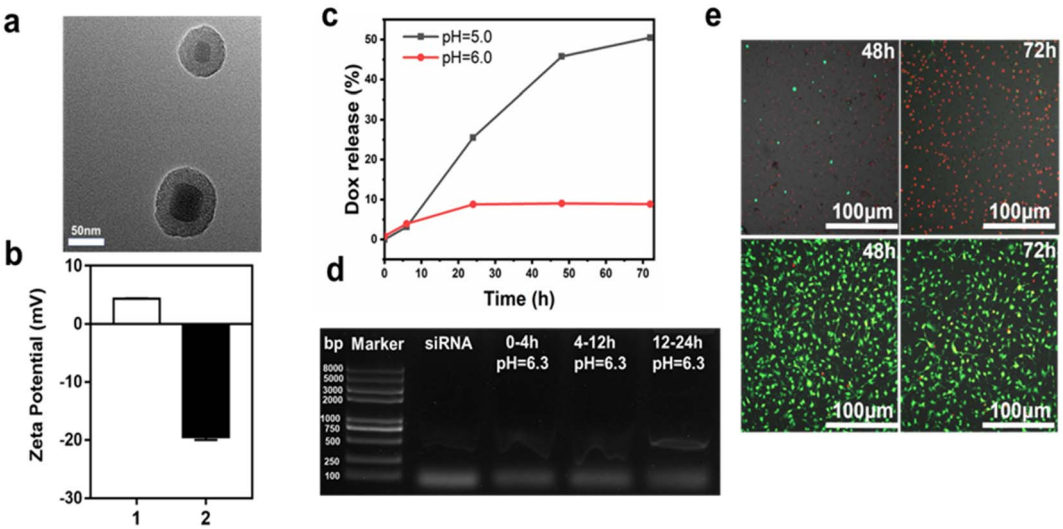

Fig. 4 Characterization of the UCNPs@mSiO$_2$@TA–Al and the sustained-release properties of the anti-cancer drug. (a) TEM analysis of UCNPs@mSiO$_2$, scale bar: 50 nm. (b) Zeta potentials analysis (1: UCNPs@mSiO$_2$–NH$_2$; 2: UCNPs@mSiO$_2$@TA–Al). (c) The cumulative release of Dox of the UCNPs@mSiO$_2$–Dox@TA–Al in different pH (5.0, 6.0) buffers; (d) a sustained release of siRNA in PBS (pH 6.3) solution containing UCNPs@mSiO$_2$@siRNA@TA–Al occurred within 4 h, followed by 8 and 12 h time intervals. (e) Calcein-AM/PI co-staining to visualise the anti-cancer activity of UCNPs@mSiO$_2$–Dox@TA–Al (100 μg mL^{-1}) in GL261 cells; up panels: UCNPs@mSiO$_2$–Dox@TA–Al groups; down panels: PBS groups.

Table 2 ICP-MS analysis of UCNPs@mSiO$_2$@TA–Al

ICP-MS	Si	Al
Atomic weight (g mol^{-1})	27	28
Mass (ppm)	410.9	9.758
Molar (mM)	14.675	0.3614

μg Al, serving as confirmation that Al was attached to UCNPs@mSiO$_2$ (Table 2). Moreover, the zeta potential of the APTES-modified UCNPs@mSiO$_2$ was measured to be +4.33 mV and UCNPs@mSiO$_2$@TA–Al reversed the potential (−19.53 mV) because of the TA–Al complex (Fig. 4b). Furthermore, the results successfully confirmed the attachment of TA–Al onto the UCNPs@mSiO$_2$. The XRD spectrum of the UCNPs@mSiO$_2$@-TA–Al is consistent with the standard card of β-NaYF$_4$ (JCPDS no. 16-0334) and the Al (JCPDS 04-0787), which verified the existence of β-NaYF$_4$ and Al. (Fig. S9†). Except for drug loading, the above nanoparticle was considered suitable for imaging through fluorescence measurements conducted with a 980 nm laser. No obvious change in the upconversion fluorescence emission spectra wavelength and sharpness were observed before and after coating TA-Al dots on the surface of UCNPs@mSiO$_2$ (Fig. S10†).

The UCNPs@mSiO$_2$@Dox@TA–Al exhibited sustained drug release. The cumulative release of Dox in the nanoparticles was assessed in two PBS solutions with different pH values (pH 5.0, 6.0). The cumulative release amount of Dox reached 50.5% at pH 5.0 within 72 h, and a remarkable pH-dependent profile was recorded. The lower pH (5.0) has a faster rate of Dox release compared with the pH of 6.0, which might be attributed to the faster decomposition rate of TA–Al under a lower pH (Fig. 4c). Moreover, the therapeutic siRNA-loaded nanospheres (UCNPs@mSiO$_2$–siRNA@TA–Al) presented a sustained release at pH 6.3, which occurred within 4 h, followed by 8 and 12 h time intervals (Fig. 4d). It is worth recalling that the siRNA easily subsided under a lower pH (<6.0), so the TA–Al may be a perfect "gatekeeper" for pH-triggered siRNA delivery. Hence, customized drug delivery can be achieved in a long time. Next, the biocompatibility of UCNPs@mSiO$_2$@TA–Al was assessed by the CCK-8 assay. After 24 h, 83.8% of NIH-3T3 cells were alive in the presence of the UCNPs@mSiO$_2$@TA–Al nanoparticles (100 μg mL^{-1}) (Fig. S11†). The good biocompatibility of the UCNPs@mSiO$_2$@TA–Al may be owning to the nontoxic properties of the TA–Al. Next, we evaluated the anti-cancer effects with UCNPs@mSiO$_2$–Dox@TA–Al (100 μg mL^{-1}) using calcein-AM/PI co-staining; most of the GL261 cells were inhibited, as shown in Fig. 4e and S12.† These results indicate that our as-synthesized UCNPs@mSiO$_2$@TA–Al nanoparticle is suitable for drug loading and cancer therapy.

Discussion

With the rapid advances in nanotechnology in recent years, many types of fluorescent probes have been designed and developed to explore their potential applications in brain tissue imaging as well as diagnosis, angiography, and other uses suitable for studying and treating brain diseases. Some examples include a single-walled carbon nanotube fluorescent probe for fluorescence imaging of mouse cerebral vessels used to penetrate the skull;[29] an organic dye probe p-fe enabled single photon-based three-dimensional confocal imaging of blood vessels in mouse brain tissue and non-invasive *in vivo* tracking of cerebrovascular blood flow in mice;[30] and a liposomal probe

consisting of a quantum dot drug mixture with efficient endocytosis into mouse bend3 cells for brain tissue imaging and therapy.[31] However, these fluorescent probes are associated with drawbacks such as toxicity, photostability, and biosafety, which limit their further applications. For example, the fluorescence emission of a single-walled carbon nanotube fluorescent probe has a broad peak (about a few hundred nanometres). Also, organic dye probes are susceptible to the interference of excited luminescence signals due to their small stokes shift, and the dye molecules themselves are also prone to photobleaching.

In contrast to the above-mentioned fluorescent probes, the emergent rare-earth NIR fluorescent probes exhibit distinct advantages such as excellent photostability and chemical stability, broad emission half peaks, long excited state lifetimes, and tuneable emission wavelengths. Impressive progress has been made in the field of bioimaging in recent years.[32–36] For example, rare-earth NIR luminescent nanomaterials developed by Zhang Fan *et al.* have shown excellent performance in imaging inflammatory lesions.[37] Huang Xiaonan *et al.* used composite nanomaterials composed of UCNPs complexed with nanographene oxide to perform excellent tumour imaging.[38] In our study, the UCNPs@Au constructed by doping with Yb^{3+} and Er^{3+} possess the UCL characteristics of rare earth ions and the nanoscale characteristics, which are less harmful to living organisms. These nanoparticles prevent the interference of background fluorescence, thereby improving the signal-to-noise ratio of images produced. These results demonstrated superior UCL imaging of the mouse brain. Also, UCNPs@Au possessed of photothermal effect to inhibit the growth of GL261 cells.

Furthermore, rare earth luminescent materials as drug carriers can also be used for delivering drugs to diseased tissues for the treatment of diseases. Combined with the differential biological endo environment between normal and diseased tissues, stimuli-responsive drug carriers can be constructed, which can release piggyback drugs under the stimulation of intrinsic environmental agents for the purpose of targeted therapy.[39,40] Micro-environmental alteration is an important mechanism leading to the occurrence and development of brain diseases.[41–44] The pH triggered formation of Aβ oligomers, increasing by a rate of 8000 folds, promoting the progression of Alzheimer's disease.[45] An acidic microenvironment has also been observed in glioblastoma, which is associated with the maintenance of stem cell properties and promotes tumour progression.[46,47] Therefore, based on the acidic microenvironment, we constructed a pH-responsive rare earth upconversion nanocarrier (UCNPs@$mSiO_2$@Dox/siRNA@TA–Al). Experimental studies *in vitro* proved that Dox released faster in lower pH (5.0) compared to pH 6.0 and most of the GL261 cells were inhibited. Moreover, the siRNA-loaded nanospheres presented a sustained release at pH 6.3. These results demonstrated TA–Al is a perfect "gatekeeper" for the pH-triggered Dox/siRNA delivery. Furthermore, UCNPs@$mSiO_2$@TA–Al nanoparticles possessed high biological security and was suitable for glioma therapy. All these results make the functionalization of UCNP a promising agent for imaging and therapy in brain disease.

Conclusions

Although rare-earth UCL nanomaterials exhibit robust imaging and drug delivery capabilities in the brain tissue, based on our present work, more in-depth and additional studies in specific animal models must be carried out in the future. Potential research studies include improvement of surface modification methods to specifically target Aβ oligomers, which will enable precision imaging in animal models of Alzheimer's disease; transport programmed death ligand 1 (PD-L1) receptors to achieve targeted immunotherapy for brain tumours; and photothermal therapy of localised brain tumour cells under light stimulation. In conclusion, rare-earth UCL nanocomposites are promising candidates for brain tissue imaging and therapy due to their ability to achieve multimodal combination therapy regimens at the nanoscale to treat brain tissue diseases.

Author contributions

Conceptualization, Hongru Wang and Yanfei Sun; methodology, Zheng Wei; software, Yangyang Zhao; validation, Hongru Wang, Zheng Wei and Yanfei Sun; formal analysis, Yangyang Zhao; investigation, Hongru Wang; resources, Shidong Wang; data curation, Kai Liu; writing—original draft preparation, Hongru Wang; writing—review and editing, Yanfei Sun; visualization, Lili Cao; supervision, Lili Cao; project administration, Fan Wang; funding acquisition, Kai Liu. All authors have read and agreed to the published version of the manuscript.

Conflicts of interest

The authors declare no conflict of interest.

Acknowledgements

This work was supported by the National Natural Science Foundation of China (Grant No. 22020102003, 22125701, 21834007, 21907088, 82202349 and 52222214), the National Key R&D Program of China (2020YFA0712102, 2018YFA0902600, and 2021YFF0701800), Beijing Natural Science Foundation (L222066), the Youth Innovation Promotion Association of CAS (Grant No. 2020228), Natural Science Foundation of Jilin Province (20210101366JC), Peking university people's Hospital research and development funds (RS2021-04).

References

1 R. Daneman and B. Engelhardt, *Neurobiol. Dis.*, 2017, **107**, 1–3.
2 C. E. Elwell, *J. Neurosurg. Anesthesiol.*, 2020, **32**, 188–190.
3 C. A. Lane, J. Hardy and J. M. Schott, *Eur. J. Neurol.*, 2018, **25**, 59–70.
4 T. Hirose, *Brain Tumor Pathol.*, 2015, **32**, 1–2.
5 Z. Breijyeh and R. Karaman, *Molecules*, 2020, **25**, 5789.
6 J. L. Cummings, G. Tong and C. Ballard, *J. Alzheimer's Dis.*, 2019, **67**, 779–794.

7 S. K. Carlsson, S. P. Brothers and C. Wahlestedt, *EMBO Mol. Med.*, 2014, **6**, 1359–1370.
8 Z. Cheng, M. Li, R. Dey and Y. Chen, *J. Hematol. Oncol.*, 2021, **14**, 85.
9 C. Ross, M. Taylor, N. Fullwood and D. Allsop, *Int. J. Nanomed.*, 2018, **13**, 8507–8522.
10 B. Formicola, A. Cox, R. Dal Magro, M. Masserini and F. Re, *J. Biomed. Nanotechnol.*, 2019, **15**, 1997–2024.
11 Z. Liu, Y. Zhu, L. Zhang, W. Jiang, Y. Liu, Q. Tang, X. Cai, J. Li, L. Wang, C. Tao, X. Yin, X. Li, S. Hou, D. Jiang, K. Liu, X. Zhou, H. Zhang, M. Liu, C. Fan and Y. Tian, *Sci. China: Chem.*, 2023, **66**, 324–366.
12 Z. Wei, Y. Liu, B. Li, J. Li, S. Lu, X. Xing, K. Liu, F. Wang and H. Zhang, *Light: Sci. Appl.*, 2022, **11**, 175.
13 X. Zhao, S. He, B. Li, B. Liu, Y. Shi, W. Cong, F. Gao, J. Li, F. Wang, K. Liu, C. Sheng, J. Su and H. G. Hu, *Nano Lett.*, 2023, **23**, 863–871.
14 L. Xiong, Z. Chen, Q. Tian, T. Cao, C. Xu and F. Li, *Anal. Chem.*, 2009, **81**, 8687–8694.
15 B. Liu, J. Sun, J. Zhu, B. Li, C. Ma, X. Gu, K. Liu, H. Zhang, F. Wang, J. Su and Y. Yang, *Adv. Mater.*, 2020, **32**, e2004460.
16 H. Chen, L. Shao, T. Ming, Z. Sun, C. Zhao, B. Yang and J. Wang, *Small*, 2010, **6**, 2272–2280.
17 W. M. Pardridge, *NeuroRx*, 2005, **2**, 3–14.
18 M. Zheng, W. Tao, Y. Zou, O. C. Farokhzad and B. Shi, *Trends Biotechnol.*, 2018, **36**, 562–575.
19 J. Li, C. W. T. Leung, D. S. H. Wong, J. Xu, R. Li, Y. Zhao, C. Y. Y. Yung, E. Zhao, B. Z. Tang and L. Bian, *ACS Appl. Mater. Interfaces*, 2019, **11**, 22074–22084.
20 F. Hu, B. Liu, H. Chu, C. Liu, Z. Li, D. Chen and L. Li, *Nanoscale*, 2019, **11**, 9201–9206.
21 G. Tian, W. Yin, J. Jin, X. Zhang, G. Xing, S. Li, Z. Gu and Y. Zhao, *J. Mater. Chem. B*, 2014, **2**, 1379–1389.
22 J. Liu, W. Bu, L. Pan and J. Shi, *Angew Chem. Int. Ed.*, 2013, **52**, 4375–4379.
23 Y. Dai, P. Ma, Z. Cheng, X. Kang, X. Zhang, Z. Hou, C. Li, D. Yang, X. Zhai and J. Lin, *ACS Nano*, 2012, **6**, 3327–3338.
24 C. Park, B. J. Yang, K. B. Jeong, C. B. Kim, S. Lee and B. C. Ku, *Angew Chem. Int. Ed.*, 2017, **56**, 5485–5489.
25 H. Ejima, J. J. Richardson, K. Liang, J. P. Best, M. P. van Koeverden, G. K. Such, J. Cui and F. Caruso, *Science*, 2013, **341**, 154–157.
26 J. Guo, Y. Ping, H. Ejima, K. Alt, M. Meissner, J. J. Richardson, Y. Yan, K. Peter, D. von Elverfeldt, C. E. Hagemeyer and F. Caruso, *Angew Chem. Int. Ed.*, 2014, **53**, 5546–5551.
27 S. L. Lin, Z. R. Chen and C. A. Chang, *Nanotheranostics*, 2018, **2**, 243–257.
28 Y. Liu, P. Bhattarai, Z. Dai and X. Chen, *Chem. Soc. Rev.*, 2019, **48**, 2053–2108.
29 G. Hong, S. Diao, J. Chang, A. L. Antaris, C. Chen, B. Zhang, S. Zhao, D. N. Atochin, P. L. Huang, K. I. Andreasson, C. J. Kuo and H. Dai, *Nat. Photonics*, 2014, **8**, 723–730.
30 H. Wan, J. Yue, S. Zhu, T. Uno, X. Zhang, Q. Yang, K. Yu, G. Hong, J. Wang, L. Li, Z. Ma, H. Gao, Y. Zhong, J. Su, A. L. Antaris, Y. Xia, J. Luo, Y. Liang and H. Dai, *Nat. Commun.*, 2018, **9**, 1171.
31 C. J. Wen, L. W. Zhang, S. A. Al-Suwayeh, T. C. Yen and J. Y. Fang, *Int. J. Nanomed.*, 2012, **7**, 1599–1611.
32 C. Hao, X. Wu, M. Sun, H. Zhang, A. Yuan, L. Xu, C. Xu and H. Kuang, *J. Am. Chem. Soc.*, 2019, **141**, 19373–19378.
33 Y. Li, C. Chen, F. Liu and J. Liu, *Mikrochim. Acta*, 2022, **189**, 109.
34 P. Jethva, M. Momin, T. Khan and A. Omri, *Materials*, 2022, **15**, 2374.
35 X. Qiu, J. Xu, M. Cardoso Dos Santos and N. Hildebrandt, *Acc. Chem. Res.*, 2022, **55**, 551–564.
36 Z. Yi, Z. Luo, X. Qin, Q. Chen and X. Liu, *Acc. Chem. Res.*, 2020, **53**, 2692–2704.
37 L. Liu, S. Wang, B. Zhao, P. Pei, Y. Fan, X. Li and F. Zhang, *Angew Chem. Int. Ed.*, 2018, **57**, 7518–7522.
38 P. Li, Y. Yan, B. Chen, P. Zhang, S. Wang, J. Zhou, H. Fan, Y. Wang and X. Huang, *Biomater. Sci.*, 2018, **6**, 877–884.
39 C. Liu, H. Chen, H. Zhou, S. Yu, N. Wang, W. Yao, A. H. Lu and W. Qiao, *ACS Appl. Mater. Interfaces*, 2021, **13**, 50716–50732.
40 S. R. MacEwan, D. J. Callahan and A. Chilkoti, *Nanomedicine*, 2010, **5**, 793–806.
41 E. Boedtkjer and S. F. Pedersen, *Annu. Rev. Physiol.*, 2020, **82**, 103–126.
42 W. Wang, Z. Lu, M. Wang, Z. Liu, B. Wu, C. Yang, H. Huan and P. Gong, *Front. Immunol.*, 2022, **13**, 998236.
43 A. M. Reuss, D. Groos, M. Buchfelder and N. Savaskan, *Int. J. Mol. Sci.*, 2021, 22.
44 Y. Lu, Z. Guo, Y. Zhang, C. Li, Y. Zhang, Q. Guo, Q. Chen, X. Chen, X. He, L. Liu, C. Ruan, T. Sun, B. Ji, W. Lu and C. Jiang, *Adv. Sci.*, 2019, **6**, 1801586.
45 M. P. Schutzmann, F. Hasecke, S. Bachmann, M. Zielinski, S. Hansch, G. F. Schroder, H. Zempel and W. Hoyer, *Nat. Commun.*, 2021, **12**, 4634.
46 N. H. Boyd, A. N. Tran, J. D. Bernstock, T. Etminan, A. B. Jones, G. Y. Gillespie, G. K. Friedman and A. B. Hjelmeland, *Theranostics*, 2021, **11**, 665–683.
47 K. D. Cortes Franco, I. C. Brakmann, M. Feoktistova, D. Panayotova-Dimitrova, S. Grunder and Y. Tian, *Pflugers Arch.*, 2023, **475**, 405–416.